Synergistic Multi-spectral CT Reconstruction with Directional Total Variation

Evelyn Cueva[1,2], Alexander Meaney[3], Samuli Siltanen[3], Matthias J. Ehrhardt[4]

[1]Research Center on Mathematical Modeling (MODEMAT), Escuela Politécnica Nacional, Quito, Ecuador

[2]Facultad de Ciencias Agropecuarias y Recursos Naturales, Universidad Técnica de Cotopaxi, Latacunga, Ecuador

[3]Department of Mathematics and Statistics, University of Helsinki, Finland

[4]Institute for Mathematical Innovation, University of Bath, United Kingdom

E-mail: evelyn.cueva1072@utc.edu.ec

Abstract. This work considers synergistic multi-spectral CT reconstruction where information from all available energy channels is combined to improve the reconstruction of each individual channel, we propose to fuse this available data (represented by a single sinogram) to obtain a polyenergetic image which keeps structural information shared by the energy channels with increased signal-to-noise-ratio. This new image is used as prior information during the minimization process through the directional total variation. We analyze the use of directional total variation within variational regularization and iterative regularization. Our numerical results on simulated and experimental data show significant improvements in terms of image quality and in computational speed.

Keywords: undersampled data, multi–energy CT, directional total variation, linearized Bregman iteration, high-resolution reconstruction.

1. Introduction

1.1. Undersampling in multi-spectral CT

Computed tomography (CT) is a widely used technique in many different fields of science and industry; for example in medicine, it enables visualizing the internal structure of a patient. The principle of this technique is to study the attenuation of X-rays when they pass through the target object [40, 8]. Despite the potential usefulness of CT, the X-ray source produces a single energy spectrum and the detector does not discriminate between photon energies. As a consequence, two tissues whose elemental composition are different might be indistinguishable in the resulting CT image [49, 50, 38]. The latter makes it difficult to identify and classify different tissues and motivates the multi-spectral techniques based on new scanner technologies [35, 2, 36].

Dual and multi-spectral CT use different technical approaches for acquiring multi-energetic data, *e.g.*, the rapid tube potential switching, multilayer detectors, or dual (multi) X-ray sources [59, 56, 32, 29]. This multi-energetic data provides much more information about the tissue composition allowing to differentiate its constituent materials [38] but, in addition, the measurement process needs a balance between radiation dose, acquisition time and image quality. A reduction in radiation dose is achieved by reducing the number of views in the acquisition which, in turn, decreases the spatial resolution [37, 23, 34]. A recent study proposes to reconstruct a multi-spectral CT image by reducing the dose in each energy window, when just a limited and non-overlapping range of angles is observed [52]. As the resolution of the reconstructions is affected by this lack of measurements, small objects cannot be reconstructed and the resulting images are affected by the presence of artifacts [28, 20]. Many advanced reconstruction techniques have been proposed to simultaneously or independently reconstruct an spectral-image in this scenario [21, 31, 41, 55, 52, 27]. For example, variational methods are commonly used since they allow to directly incorporate prior information and constraints into the model [47]. In addition, regularizers can be added as part of the objective functional or in the optimization process, to overcome ill-posedness [46]. The expected structural correlation between different energy levels has motivated the use of structural priors to improve these reconstructions [30, 43, 31, 25, 52], some of them based on level sets methods [15]. For example, in [31] the structural information has been added using directional total variation. This regularizer has been successfully used in several other medical imaging applications [17, 16, 18] and hyperspectral remote sensing [7].

1.2. Main contribution

We propose a novel reconstruction technique to solve the undersampling problem in multi-spectral CT, where information from all available energy channels is combined to obtain a polychromatic image. The latter keeps the structural information shared by the energy channels and is used to improve the reconstruction of each individual channel using directional total variation (dTV). We explore variational and iterative regularization methods, specifically, the forward-backward splitting algorithm (FBS) [12, 11] and Linearized Bregman iterations [42, 57, 58, 5, 13] to solved the undersampling problem using simulated and experimental data. The combination of these methods and dTV show improvements in terms of image quality and computational speed.

In section 2, we describe the inverse problem behind multi-spectral CT data seen as a minimization problem. Later, in section 3, we present the variation and iterative regularization of the inverse problem and we describe the FBS algorithm and Bregman iterations to solved them,respectively. We include total variation and directional total variation regularizers to be included during the regularization process. th all the parameters that we consider during the optimization process. The last section is devoted to present numerical results using synthetic and real data. Here, we specify all the settings needed during the reconstruction.

2. Inverse problem

Multi-spectral CT aims to recover energy-dependent attenuation maps $\boldsymbol{u}_k$ of a target object for energies E_k with $k = 1, ..., K$. The acquisition method considers X-ray projections using only a limited set of angles, *i.e.*, we want to reconstruct $\boldsymbol{u}_k \in \mathbb{R}^N$ given data $\boldsymbol{b}_k \in \mathbb{R}^M$ where $M \ll N$. When a considerable amount of measurements is available, classical methods such as filtered back projection, Kaczmarz iterations or iterative techniques can be used to solve an associated linear system of the form $A\boldsymbol{u}_k = \boldsymbol{b}_k$ or the associated least squares problem (see *e.g.* [40, 9])

$$\min_{\boldsymbol{u}_k \in \mathbb{R}^N} \frac{1}{2} \|A\boldsymbol{u}_k - \boldsymbol{b}_k\|_2^2, \tag{2.1}$$

where A is the forward operator (a matrix in the discrete case) that relates the image $\boldsymbol{u}_k$ to the given data $\boldsymbol{b}_k$. The ill-posedness of this inverse problem makes a direct inversion of the matrix A unstable even for a suitable number of measurements. The undersampling scenario is even more challenging, since $M \ll N$, the system is under-determined.

For 2D CT, $M = m_1 \cdot m_2$ where m_1 is the number of angles and m_2 is the number of detectors, and $N = n_1 \cdot n_2$, where n_1 and n_2 are the number of rows and columns of $\boldsymbol{u}_k$ (considered as a matrix of pixels), respectively.

2.1. Forward model

We recall the forward modelling for multi-spectral CT. For a fixed energy channel E_k, an initial intensity $I_i^0(E_k)$ of X-rays is emitted along a line L_i (from source to detector) given a final intensity I_i^1, for $i = 1, \dots M$. The discretized linear model use for reconstructing a vectorized image $\boldsymbol{u}(E_k)$ of N pixels (see, *e.g* [31]) is given by

$$b_{ik} := -\ln\left(\frac{Z_{ik}}{I_i^0(E_k)}\right) \approx \sum_{j=1}^{N} a_{ij} u_j(E_k). \tag{2.2}$$

where our measurements are Poisson distributed with expectation $I_i^1(E_k)$, *i.e.*

$$Z_{ik} \sim \text{Poiss}\{I_i^1(E_k)\}, \quad i = 1, \dots, M, \quad k = 1, \dots, K.$$

In (2.2), $u_j(E_k)$ is the value of $\boldsymbol{u}(E_k)$ in the corresponding pixel j, and a_{ij} is the length of the intersection of the i-th line and the j-th pixel.

Based on the discretization presented above for each energy E_k, we establish a linear system that allows us to recover $u_j(E_k)$ for all $j = 1, \dots, N$, namely

$$A_k \boldsymbol{u}_k = \boldsymbol{b}_k, \qquad k = 1, \dots, K, \tag{2.3}$$

where $A_k \in \mathbb{R}^{M \times N}$, is a matrix with components a_{ij}. The vector $\boldsymbol{u}_k \in \mathbb{R}^N$ with components u_j and, $\boldsymbol{b}_k$ is the vector of measurements b_{ik} for the fixed energy level k. The matrix A_k represents the discretization of the X-ray transform for a particular projection geometry.

From now on, we omit the energy sub-index in (2.3) since we will solve an independent problem for each energy channel.

3. Regularization

In this section we discuss the regularizers used in this work, total variation and directional total variation, and how these can be used to regularize an inverse problem. To this end we consider variational regularization and iterative regularization based on Bregman iterations.

3.1. Regularizers

3.1.1. Total Variation The total variation (TV) regularization has been widely studied due to its edge-preserving properties [45]. The TV regularizer is defined as the 1-norm of a discrete finite difference approximation of the gradient $\nabla\colon \mathbb{R}^N \to (\mathbb{R}^2)^N$, namely

$$\text{TV}(\boldsymbol{u}) = \|\nabla \boldsymbol{u}\|_{2,1} = \sum_{j=1}^{N} \left(|\nabla_1 \boldsymbol{u}_j|^2 + |\nabla_2 \boldsymbol{u}_j|^2\right)^{1/2}.$$

The TV regularizer is well-known to promote piecewise constant images with sharp edges.

3.1.2. Directional Total Variation While TV is a powerful regularizer, it is unclear how additional structural a-priori information can be included. To this end we utilize the directional total variation (dTV) proposed in [16]. Let $\boldsymbol{\xi} \in (\mathbb{R}^2)^N$ be a vector field with $\|\boldsymbol{\xi}_i\| \leq \eta < 1$. We denote by $\mathbf{P} \in (\mathbb{R}^{2\times 2})^N$, $\mathbf{P}_i := \mathbf{I} - \boldsymbol{\xi}_i \otimes \boldsymbol{\xi}_i$ an associated matrix-field, where $\mathbf{I}$ is the 2×2 matrix and $\otimes$ represents the outer product of vectors. Then $\mathrm{dTV}\colon \mathbb{R}^N \to \mathbb{R}$ is defined as

$$\mathrm{dTV}(\boldsymbol{u}; \boldsymbol{v}) = \sum_j \|\mathbf{P}_j \nabla \boldsymbol{u}_j\|, \tag{3.1}$$

where $\mathbf{P}_j$ implicitly depends on $\boldsymbol{v}$ by means of $\boldsymbol{\xi}$.

Some interpretations of dTV are detailed in [17, 7]. We briefly describe some useful properties of this functional using the explicit expression $\mathbf{P}_j \nabla \boldsymbol{u}_j = \nabla \boldsymbol{u}_j - \langle \boldsymbol{\xi}_i, \nabla \boldsymbol{u}_j \rangle \boldsymbol{\xi}_i$. We observe two particular cases:

$$\mathbf{P}_j \nabla \boldsymbol{u}_j = \begin{cases} (1 - \|\boldsymbol{\xi}_j\|^2) \nabla \boldsymbol{u}_j, & \text{if } \nabla \boldsymbol{u}_j \text{ is parallel to } \boldsymbol{\xi}_j \\ \nabla \boldsymbol{u}_j, & \text{if } \nabla \boldsymbol{u}_j \text{ is perpendicular to } \boldsymbol{\xi}_j. \end{cases}$$

So, when we minimize $\mathrm{dTV}(\boldsymbol{u})$, we are favouring $\boldsymbol{u}$ such that its gradient is collinear to the direction $\boldsymbol{\xi}_i$ as long as $\|\boldsymbol{\xi}_i\| \neq 0$. We note that a vanishing gradient $\nabla u = 0$ always leads to a smaller function value such that no artificial jumps are enforced.

In order to incorporate dTV into our model, we define the vector field below based on the known image $\boldsymbol{v} \in \mathbb{R}^N$ by

$$\boldsymbol{\xi}_j = \eta \frac{\nabla \boldsymbol{v}_i}{\|\nabla \boldsymbol{v}_i\|_\varepsilon} \tag{3.2}$$

with $\|\boldsymbol{u}\|_\varepsilon = \sqrt{\|\boldsymbol{u}\|^2 + \varepsilon^2}$. The parameter $\varepsilon > 0$ avoids singularities when $\nabla \boldsymbol{v}_i = 0$ and η is an edge parameter related to the size of an edge.

Figure 1 shows an example which compared TV and dTV. In contrast to TV, dTV only penalizes edges which are missing in the side information.

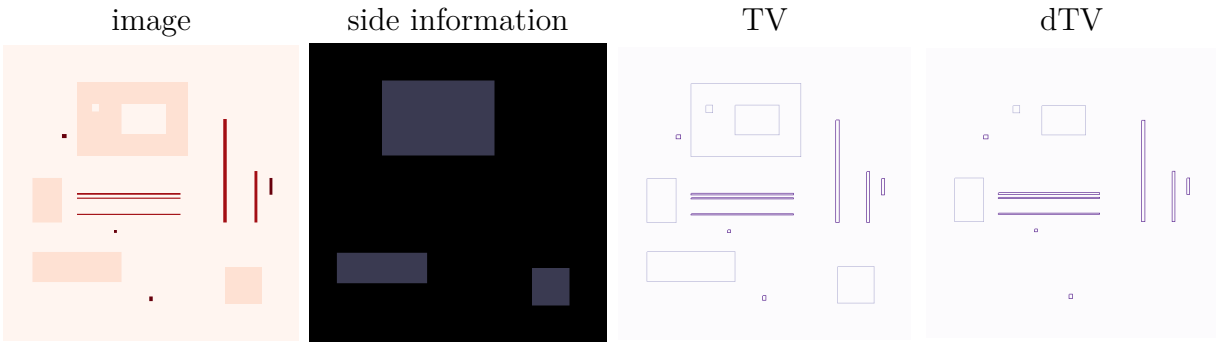

Figure 1. *From left to right:* An image $\boldsymbol{u}$, side information $\boldsymbol{v}$, pointwise TV-norm $j \mapsto \|\nabla u_j\|$, and pointwise dTV-norm $j \mapsto \|\mathbf{P}_j \nabla \boldsymbol{u}_j\|$ as in (3.1).

3.2. Variational regularization

A strategy to reconstruct $\boldsymbol{u} := \boldsymbol{u}_k$ in (2.3) is to solve

$$\boldsymbol{u}^* \in \arg\min_{\boldsymbol{u}\in\mathbb{R}^N} \left\{ \frac{1}{2}\|A\boldsymbol{u} - \boldsymbol{b}\|_2^2 + \alpha J(\boldsymbol{u}) + \iota_{[0,\infty)^N}(\boldsymbol{u}) \right\}. \tag{3.3}$$

The first term in (3.3) is called the data-fit and forces $A\boldsymbol{u}$ to stay close to the data, and the regularizer J promotes stability of the inversion. The parameter $\alpha > 0$ balances the data-fit term and the regularization provided by J. We will use TV and dTV as J. The additional term $\iota_{[0,\infty)^N}(\boldsymbol{u})$ is included to impose a nonnegativity constraint for each component of the solution $\boldsymbol{u}^*$ and is defined as:

$$\iota_{[0,\infty)^N}(\boldsymbol{u}) = \begin{cases} 0, & \text{if } u_j \geq 0 \\ \infty, & \text{otherwise.} \end{cases}$$

Depending on the type of regularization that we choose, we define the following functions:

$$G_{\mathrm{TV}}(\boldsymbol{u}) \;= \alpha\,\mathrm{TV}(\boldsymbol{u}) + \iota_{[0,\infty)}(\boldsymbol{u}), \tag{3.4}$$

$$G_{\mathrm{dTV}}(\boldsymbol{u}) = \alpha\,\mathrm{dTV}(\boldsymbol{u}, \boldsymbol{v}) + \iota_{[0,\infty)}(\boldsymbol{u}). \tag{3.5}$$

3.2.1. Forward-backward splitting algorithm The forward-backward splitting (FBS) algorithm [12] solves the composite minimization problem

$$\min_{\boldsymbol{u}} \{F(\boldsymbol{u}) + G(\boldsymbol{u})\} \tag{3.6}$$

where $F\colon X \to \mathbb{R}$ and $G\colon X \to (-\infty, \infty]$ are two proper, lower semi-continuous and convex functionals such that F is differentiable on X with a L-Lipschitz continuous gradient for some $L \in (0, \infty)$.

The principle of this algorithm is based on the two following steps:

(i) a forward (explicit) gradient step on F, *i.e.* $\boldsymbol{u}^{t+1/2} = \boldsymbol{u}^t - \sigma^t \nabla F(\boldsymbol{u}^t)$, and

(ii) a backward (implicit) step involving only G, *i.e.* $\boldsymbol{u}^{t+1} = \mathrm{prox}_{\sigma^t G}(\boldsymbol{u}^{t+1/2})$, where the proximal operator is given by

$$\mathrm{prox}_{\sigma G}(\boldsymbol{z}) = \arg\min_{\boldsymbol{y}} \left\{ \frac{1}{2}\|\boldsymbol{y} - \boldsymbol{z}\|^2 + \sigma G(\boldsymbol{y}) \right\}. \tag{3.7}$$

The step size σ^t is chosen in each iteration so that it satisfies the descent inequality

$$F\left(\boldsymbol{u}^{t+1}\right) \leq F\left(\boldsymbol{u}^t\right) + \left\langle \nabla F\left(\boldsymbol{u}^t\right), \boldsymbol{u}^{t+1} - \boldsymbol{u}^t \right\rangle + \frac{1}{2\sigma^t}\|\boldsymbol{u}^{t+1} - \boldsymbol{u}^t\|^2. \tag{3.8}$$

More precisely, we reduce σ^t until the condition (3.8) is satisfied. This selection of σ is known as *backtracking* and is considered in FBS and Bregman iterations.

Now, comparing problem (3.6) with (3.3), we choose the functions F and G as

$$F(\boldsymbol{u}) = \frac{1}{2}\|A\boldsymbol{u} - \boldsymbol{b}\|_2^2, \qquad G(\boldsymbol{u}) = \alpha J(\boldsymbol{u}) + \iota_{[0,\infty)^N}(\boldsymbol{u}).$$

We use the Fast Iterative Shrinkage Thresholding Algorithm (FISTA) presented in [3, 16] to compute the proximal operators of G_{TV} and G_{dTV} associated to the minimization problem (3.7). In this way, we ask the algorithm to have warm started FISTA iterations or to stop when a given tolerance is reached. Additionally, we define the objective function value at point $\boldsymbol{u}$ as $H(\boldsymbol{u}) = F(\boldsymbol{u}) + G(\boldsymbol{u})$. Since FBS algorithm converges to a minimizer of H [12], we stop the algorithm when the difference between two consecutive iterations of the H value is less than a given tolerance tol, *i.e.* $H(\boldsymbol{u}^{t+1}) - H(\boldsymbol{u}^t) \leq \mathrm{tol} \cdot H(\boldsymbol{u}^{t+1})$. The algorithm 1 describes one iteration of FBS algorithm.

Algorithm 1 An iteration of forward-backward splitting algorithm

$\boldsymbol{u}^{t+1} = \mathrm{prox}_{\sigma^t G}\left(\boldsymbol{u}^t - \sigma^t \nabla F(\boldsymbol{u}^t)\right).$
if $F(\boldsymbol{u}^{t+1}) > F(\boldsymbol{u}^t) + \langle \nabla F(\boldsymbol{u}^t), \boldsymbol{u}^{t+1} - \boldsymbol{u}^t \rangle + \frac{1}{2\sigma^t}\|\boldsymbol{u}^{t+1} - \boldsymbol{u}^t\|^2$ **then**
    $\sigma^t = \underline{\rho}\sigma^t$, for any $\underline{\rho} < 1$ and go back to Step 2.
else
    $\sigma^{t+1} = \overline{\rho}\sigma^t$, for any $\overline{\rho} > 1$.
end if

3.3. Iterative regulatization

A different way to achieve regularization is to apply an iterative method to directly solve the problem (2.1). Iterative methods start with a some vector $\boldsymbol{u}^0$ and generate a sequence $\boldsymbol{u}^1, \boldsymbol{u}^2, \ldots$ that converges to some solution. Usually in these methods, initial iterates $\boldsymbol{u}^t$ are fairly close to the exact solution. However, for later iterations, the solutions start to diverge from the desired one and tend to converge to the naive solution $A^{-1}\boldsymbol{b}$. Thus, the success of these methods relies on stopping the iterations at the right time. This behavior is known as *semiconvergence* [24, 40] and it is a frequently used tool to solve large-scale problems. In figure 2 we present an example of this effect. Additionally, iterative regularization avoids a predetermined regularization parameter, and instead, the number of iterations takes the role of a regularization parameter [24]. This is an advantage compared to variational regularization since in this latter, a minimization problem needs to be solved every time that a new regularization parameter α is tested.

3.3.1. Linearized Bregman iterations Under this group of iterative methods, we explore the Linearized Bregman iterations. This algorithm allows us to solve the least squares problem (2.1).

We consider the (linearized) Bregmen iterations [42, 58] which makes use of the Bregman distance defined in terms of a given functional J by

$$D_J^{\boldsymbol{q}^t}(\boldsymbol{u}, \boldsymbol{u}^t) = J(\boldsymbol{u}) - J(\boldsymbol{u}^t) - \langle \boldsymbol{q}^t, \boldsymbol{u} - \boldsymbol{u}^t \rangle,$$

where $\boldsymbol{q}^t \in \partial J(\boldsymbol{u}^t)$ is an element of the sub-differential of J at point $\boldsymbol{u}^t$.

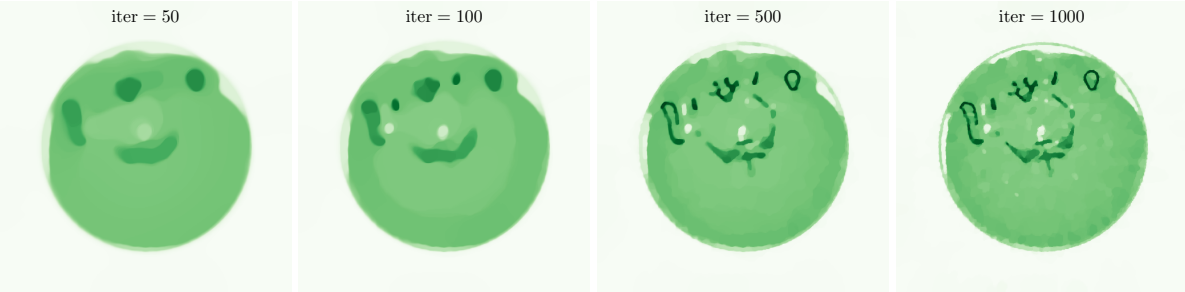

Figure 2. Iterations along the Linearized Bregman iterations. While early iterations are very smooth, the iterates become gradually better defined and eventually the measurement noise is introduced.

Linearized Bregman iterations are defined as

$$\boldsymbol{u}^{t+1} = \text{prox}_{\sigma^t G}\left(\boldsymbol{u}^t + \sigma^t(\boldsymbol{q}^t - \nabla F(\boldsymbol{u}^t))\right) \tag{3.9}$$

$$\boldsymbol{q}^{t+1} = \boldsymbol{q}^t - \frac{1}{\sigma^t}\left(\boldsymbol{u}^{t+1} - \boldsymbol{u}^t + \sigma^t \nabla F(\boldsymbol{u}^t)\right) \tag{3.10}$$

where $F(\boldsymbol{u}) = \frac{1}{2}\|A\boldsymbol{u} - \boldsymbol{b}\|_2^2$ is the objective function value and G can be chosen as G_{TV} or G_{dTV} from (3.4) and (3.5), respectively. The algorithm with backtracking is detailed in algorithm 2.

Algorithm 2 An iteration of Linearized Bregman iterations.

$\boldsymbol{u}^{t+1} = \text{prox}_{\sigma^t G}(\boldsymbol{u}^t + \sigma^t(\boldsymbol{q}^t - \nabla F(\boldsymbol{u}^t)))$
if $F(\boldsymbol{u}^{t+1}) > F(\boldsymbol{u}^t) + \langle \nabla F(\boldsymbol{u}^t), \boldsymbol{u}^{t+1} - \boldsymbol{u}^t \rangle + \frac{1}{2\sigma^t}\|\boldsymbol{u}^{t+1} - \boldsymbol{u}^t\|^2$ **then**
    $\sigma^t = \underline{\rho}\sigma^t$, for any $\underline{\rho} < 1$ and go back to Step 2.
else
    $\sigma^{t+1} = \overline{\rho}\sigma^t$, for any $\overline{\rho} > 1$.
end if

4. Numerical results

We consider two sets of data, the first one, related to real measured data and a second one using synthetic (simulated) data. In both cases, we consider three energies labeled as E_0, E_1 and E_2, which are reconstructed separately. We analyze each energy channel independently as individual optimization problems. We compare the results forward-backward splitting and linearized Bregman iterations and, highlight the main differences between TV and dTV regularizers. These algorithms were implemented using Python programming language and the Operator Discretization Library (ODL) [1]. For each energy channel, we consider sinograms of size 90×552, *i.e.* 90 projection angles and 552 detectors. These angles are uniformly distributed in the interval $[0, 2\pi)$ and the reconstructed images $\boldsymbol{u}$ are of size 512×512.

First, we detail how to choose the side information $\boldsymbol{v}$ in our experiments considering the multi-spectral information in each energy channel.

4.0.1. Choice of side information We propose to reconstruct a polyenergetic image $\boldsymbol{v} \in \mathbb{R}^N$ based on combining the data sets $\boldsymbol{b}_k \in \mathbb{R}^M$ for $k \in \{1, 2, 3\}$, *i.e.*, we solve

$$\boldsymbol{v} \in \operatorname*{arg\,min}_{\boldsymbol{u} \in \mathbb{R}^N} \left\{ \frac{1}{2} \|A\boldsymbol{u} - \tilde{\boldsymbol{b}}\|_2^2 + \alpha \, \mathrm{TV}(\boldsymbol{u}) + \iota_{[0,\infty)^N}(\boldsymbol{u}) \right\}. \tag{4.1}$$

where $\tilde{\boldsymbol{b}} = \sum_{k=1}^{3} \boldsymbol{b}_k$. The regularization parameter α and more details related to this optimization problem will be specified during the numerical experiments for synthetic and real data. Solving (4.1), we get an image $\boldsymbol{v}$ that despite of losing the spectral resolution, keeps structural information provided by all energy levels. Additionally, this image has higher signal-to-noise ratio and helps to improve the individual reconstructions $\boldsymbol{u}_k$ as we show in our experiments.

We present the results using red, green and blue color maps for E_0, E_1 and E_2, respectively. We use the color grey to distinguish everything related to side information, making an analogy with the grayscale representation of an RGB image.

4.1. Real data experiments

Experimental data was gathered at the Department of Physics, University of Helsinki, using a cone-beam micro-CT scanner with an end-window tube and a tungsten target (GE Phoenix nanotom 180 NF). The chest of a small bird was used as a test phantom, as it contains multiple different tissue types as well as fine details arising from the bone structure. The bird phantom was imaged using three different X-ray tube settings in the same geometry. 2D sinograms were created using the central plane of the cone-beam projections, in which the geometry reduces to a fan-beam geometry. First, we discuss about the choice of reference images and side information.

Reference images: The reference images are reconstructions from data with 720 angles and 552 detectors, computed via (3.3) using FBS and TV regularizer. The regularization parameter α is chosen to preserve low noise and high-resolution details in each energy channel, see in figure 3.

Choice of side information: We solve the problem (4.1) for different values of α, we compare the resulting reconstructions in figure 4. We chose the reconstruction with $\alpha = 0.03$, that keeps sharper boundaries and includes few artifacts during the reconstruction. We will compare the results obtained for two different side information images in synthetic data section (see figure 16).

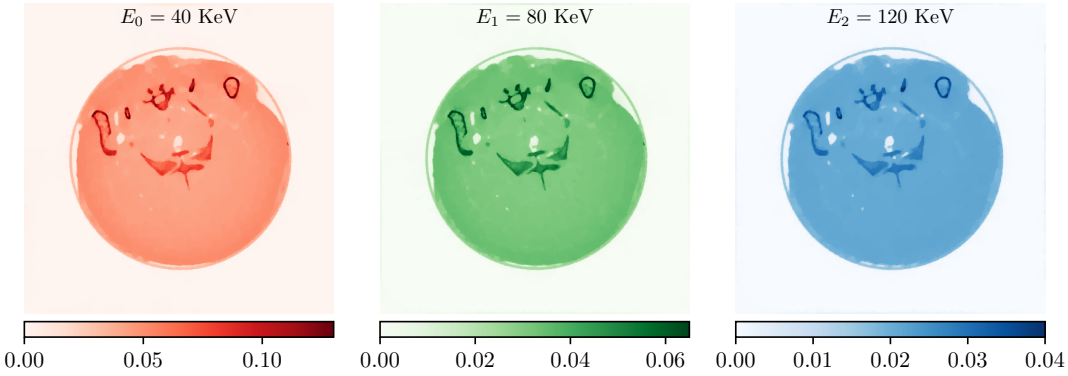

Figure 3. Reference images for real data solving the problem (3.3) with $\alpha = 0.005$, $\alpha = 0.002$ and $\alpha = 0.002$ for E_0, E_1 and E_2,respectively.

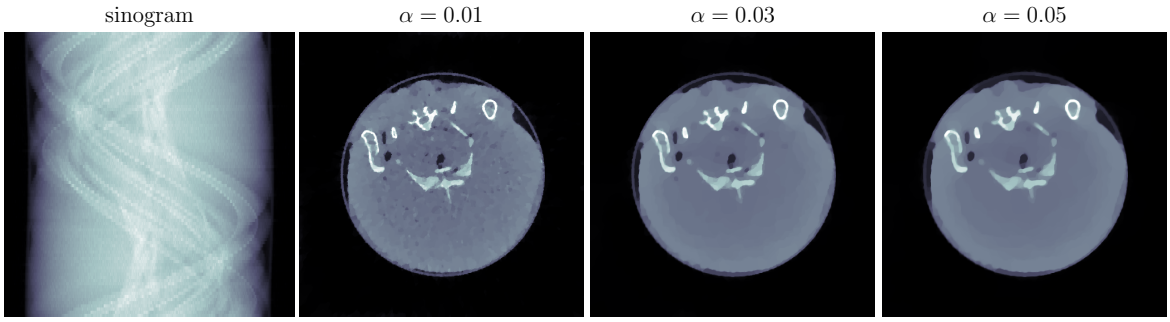

Figure 4. From left to right: sinogram of the prior information with 90 angles and 552 detectors, TV solutions of the problem (3.3) with $\alpha = 0.01$, $\alpha = 0.03$ and $\alpha = 0.05$, respectively. The minimization problem is solved with FBS algorithm in a space of size 512×512.

FBS results: We run the FBS iterations from algorithm 1, starting with $\boldsymbol{u}^0 = 1 \in \mathbb{R}^N$ and $\sigma^0 = 1/\|A\|^2$, where $\|A\|$ is an estimated norm of the operator A. We set tolerance as tol $= 10^{-6}$ for all the experiments, so the algorithm stops when $H(\boldsymbol{u}^{t+1}) - H(\boldsymbol{u}^t) \leq \text{tol} \cdot H(\boldsymbol{u}^{t+1})$. We choose $\eta = 0.01 \cdot \max_x |\nabla v(x)|$ for dTV definition (3.2) as commonly done for this regularizer [16, 7].

The results for all energies are shown in figure 5, we have included the structural similarity measure (SSIM) [53] and Peak Signal-to-Noise Ratio (PSNR) [26] measures implemented in ODL, to compare the quality of the reconstructions to the reference images in figure 3.

Bregman results: For algorithm 2, we start with $\sigma^0 = 1/\|A\|^2$ and $\boldsymbol{u}^0 = \boldsymbol{q}^0 = \boldsymbol{0} \in \mathbb{R}^N$. These choices guarantee that $\boldsymbol{q}^0 \in \partial G(\boldsymbol{u}^0)$ for $G = G_{\text{TV}}$ or $G = G_{\text{dTV}}$. We run 2000 iterations in algorithm 2 using $\alpha = 10$ for (3.4) and (3.5). We observe from figure 6 a common pattern along energies: the SSIM curve for TV is always below the curve associated to dTV, additionally, the number of iterations needed to maximize SSIM is always smaller for dTV than TV. The diamond markers included refer to the best iterations in terms of SSIM. The images with highest SSIM are presented in figure 7.

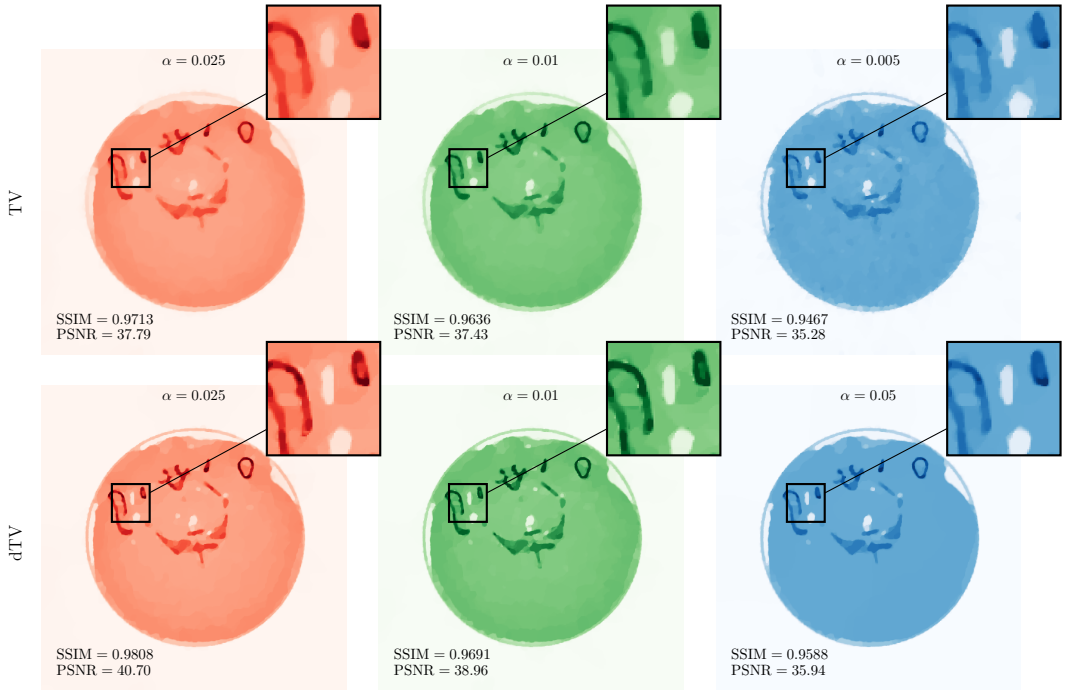

Figure 5. For the three energies, reconstructions using FBS algorithm with TV (upper row) and dTV (bottom row). For each setting, α is chosen to maximize SSIM.

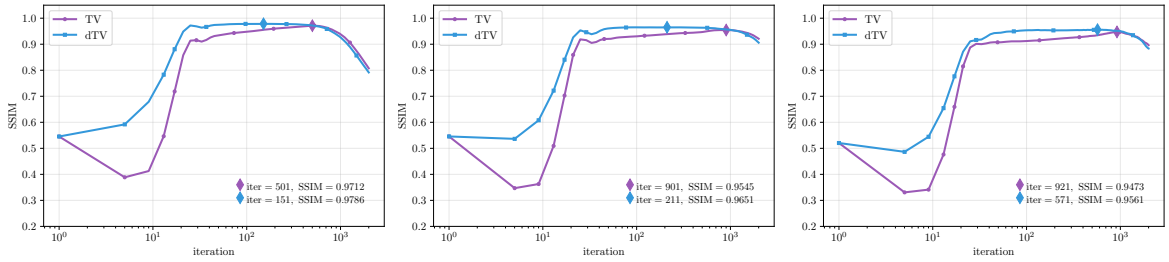

Figure 6. For each energy level, the graphs show iterations against SSIM.

Comparison between FBS and Bregman iterations: After calibration of the regularization parameter α for FBS and iteration number for Bregman iterations, we compare the two algorithms for E_0 in figure 8. We observe that both algorithms give similar values for PSNR and SSIM but consistently dTV outperforms TV.

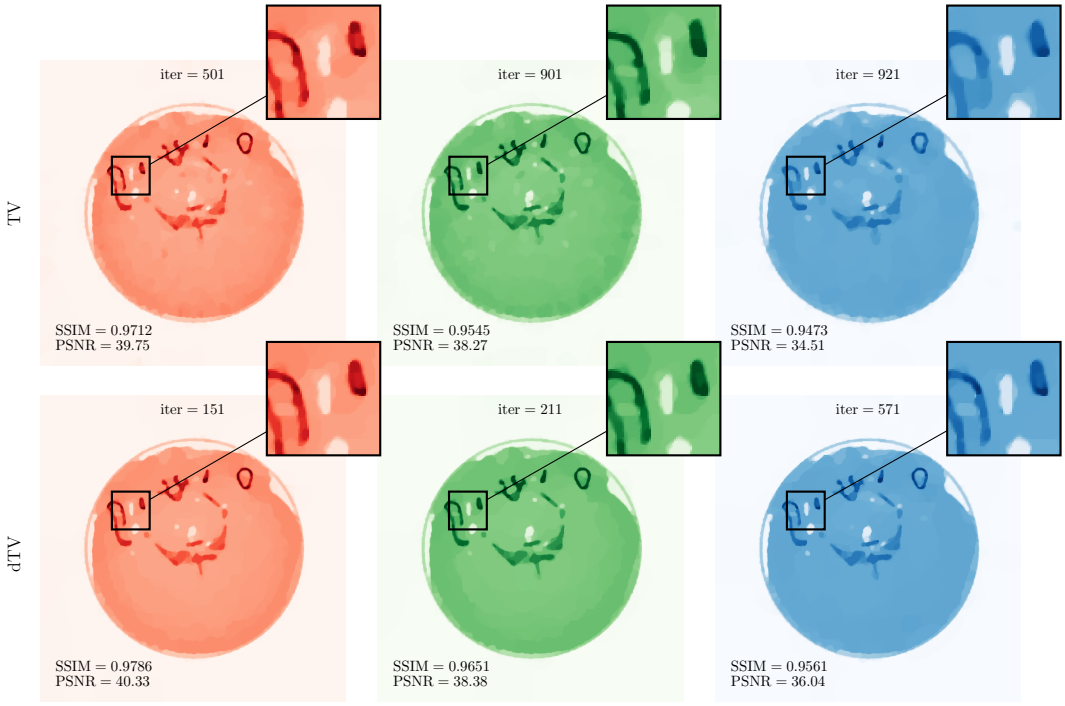

Figure 7. For the three energies, reconstructions using Bregman iterations with TV(upper row) and dTV (bottom row). Each image is labeled by the iteration that maximize SSIM.

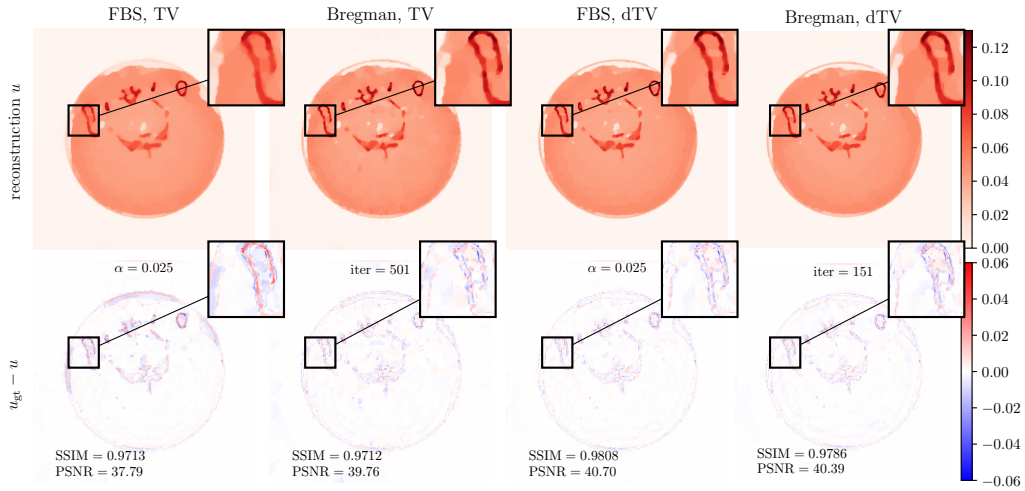

Figure 8. Top: reconstructions for E_0 using "optimal" regularization for both FBS and Bregman iterations. Bottom: difference between reconstruction and reference image (see figure 3).

4.2. Synthetic data experiments

We designed a new geometric phantom based on [31], see figure 11. Our phantom is mainly composed of three materials: quartz, pyrite and galena as shown in figure 9. As described in [31], a X-ray spectrum $q(E)$ is generated with a tube potential of $E = 120\,\text{keV}$, the obtained source spectrum is normalized $\tilde{q}(E)$ and multiplied by the initial photon flux $I_0 = 4 \times 10^7$. The resulting spectrum is shown in figure 10. We focus on three energies $E_0 = 50\,\text{keV}$, $E_1 = 85\,\text{keV}$ and $E_2 = 100\,\text{keV}$. Also figure 10 shows, we include the photon attenuation process along the energy spectrum, which determines the mass attenuation coefficient of each material at each energy channel.

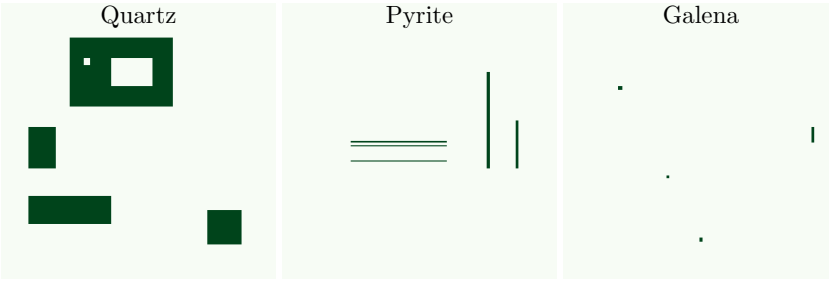

Figure 9. Materials distribution used for synthetic phantom.

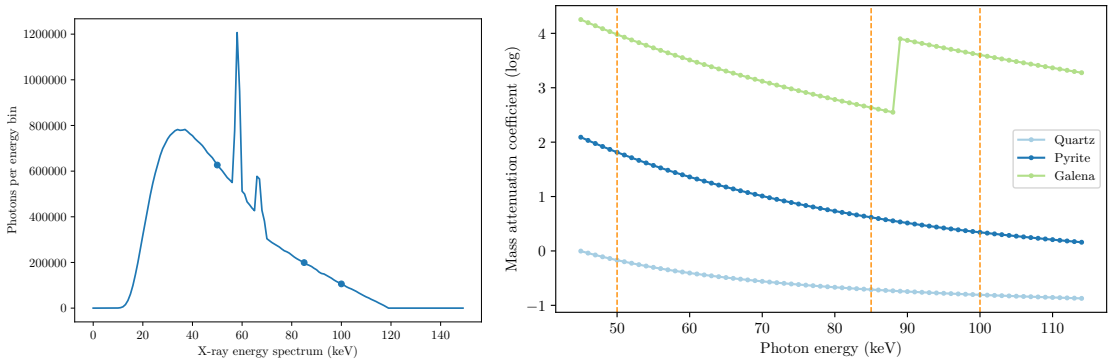

Figure 10. *Left:* The energy spectrum given by $I_0\tilde{q}(E)$. *Right:* mass attenuation curves by material. In both figures, we have pointed out the energies that are considered for our experiments.

Choice of side information: As in real case, we solve the problem (4.1) using $\alpha = 10^{-4}$, $\alpha = 5 \times 10^{-4}$ and $\alpha = 10^{-3}$. We have chosen the image with $\alpha = 10^{-4}$, which gave us the best results. We discuss the accuracy of side information choice in figure 16.

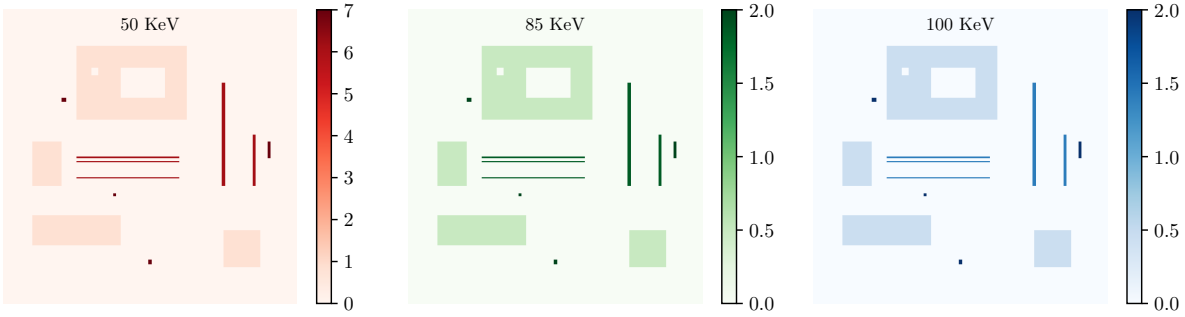

Figure 11. Reference images for $E_0 = 50\,\text{keV}$, $E_1 = 85\,\text{keV}$ and $E_2 = 100\,\text{keV}$.

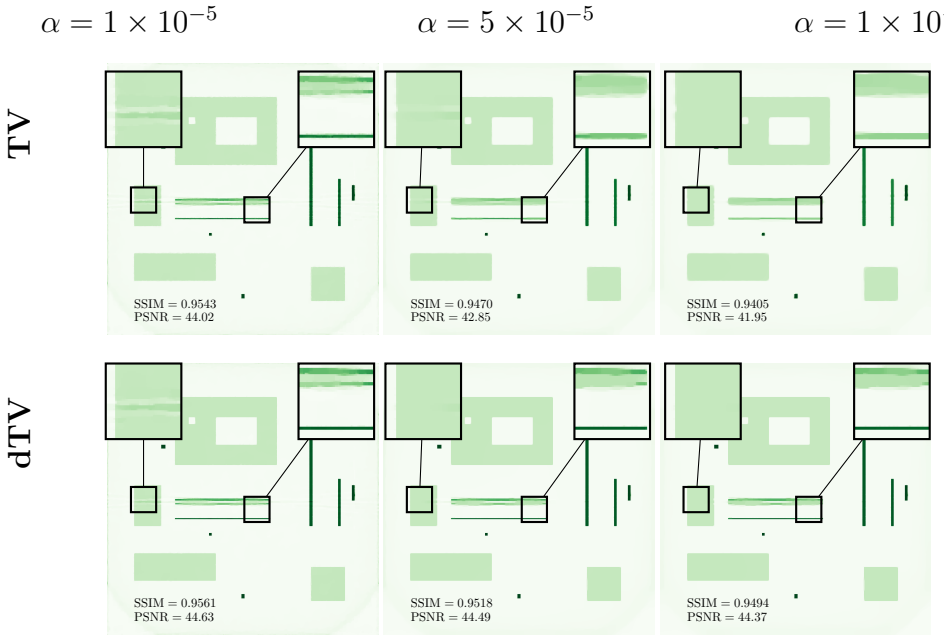

Figure 12. For E_1, reconstructions using FBS algorithm using TV (upper row) and dTV (bottom row). Each column is labeled by the α parameter used during the reconstruction.

FBS results: We initialized $\boldsymbol{u}^0$ and σ^0 as in real experiments. In figure 12, we present the results obtained for three different values of α for TV and dTV regularizers using E_1. We included close-ups for easier comparison of the reconstructions. Here, we observe that using dTV yields higher values of measures and better reconstructions reducing the artifacts in the zoomed area at the top. The same analysis is applied for the other two energies and the best choice of α is summarized in figure 13.

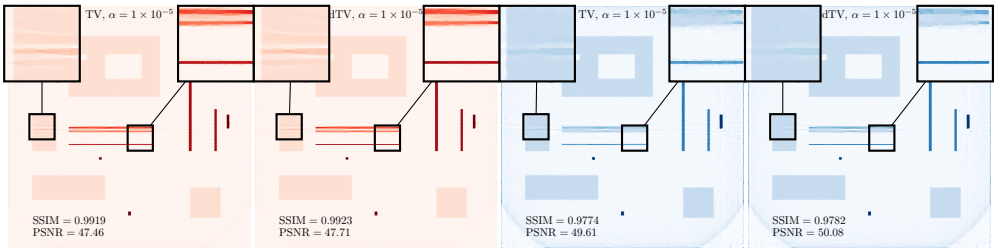

Figure 13. Best regularization parameter α for E_1 (left) and E_2 (right) for both TV and dTV.

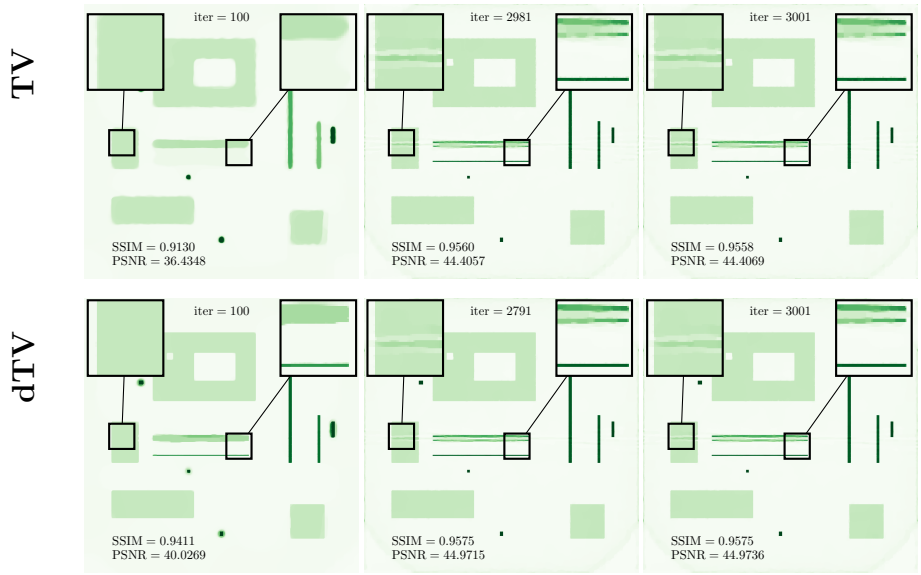

Figure 14. Bregman iterations for TV (upper row) and dTV (bottom row) in E_1. The middle image is the one with highest SSIM.

Bregman results: Now, we observe the results for algorithm 2. We initialize $\sigma^0 = 1/\|A\|^2$ and $\boldsymbol{u}^0 = \boldsymbol{q}^0 = \mathbf{0} \in \mathbb{R}^N$. We run the algorithm for 3000 iterations but using $\alpha = 0.1$ as regularizer. As before, the "optimal" iteration number is chosen to maximize SSIM. The iterations for E_1 are presented in figure 14 using TV and dTV.

The FBS and Bregman reconstructions are similar. However, we note that fewer iterations were needed for Bregman iterations to reach those reconstruction compared to FBS as shown in figure 15.

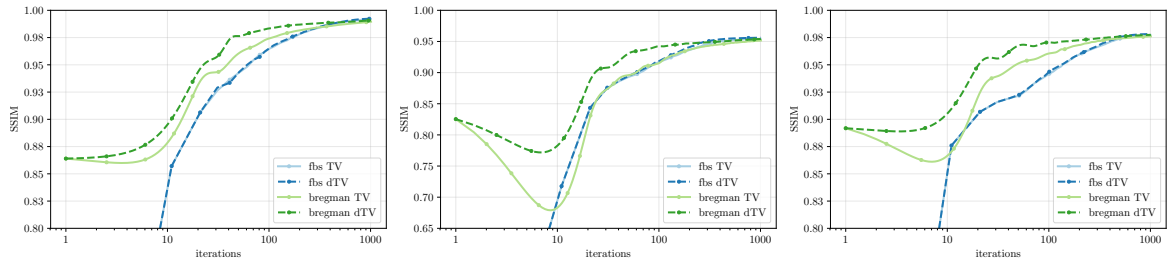

Figure 15. SSIM along iterations for fbs and Bregman iterations using both TV and dTV.

4.2.1. Influence of side information In this experiment, we compare the accuracy of the reconstructions depending on the choice of side information. For this, we consider two different regularization parameters $\alpha = 10^{-4}$ and $\alpha = 1 \times 10^{-3}$ to solve (4.1). These two choices, shown in figure 16, give us one image with sharper side information (upper row) but containing some extra features as is observed in the zoomed zones, and another image with smoother shapes with round corners (bottom row). We compare the best reconstructions using the dTV and FBS algorithms, based on the highest values of SSIM. For the second side information, some artifacts were observed, together with smaller similarity measures values and larger number of iterations for the Bregman iterations compared to the first side information.

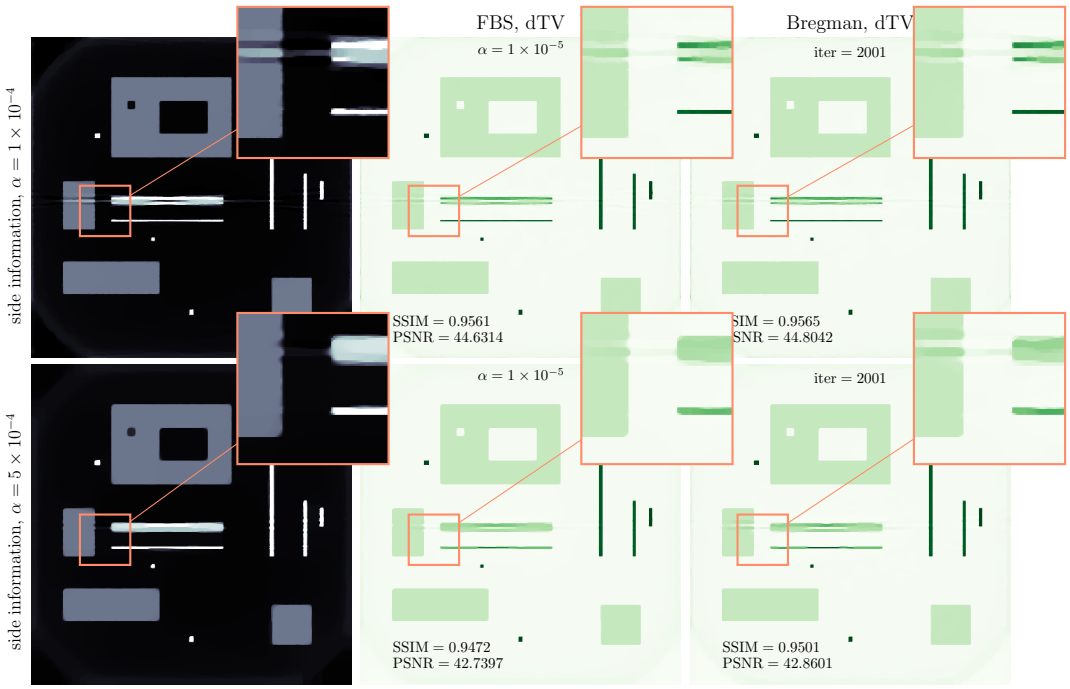

Figure 16. For two different values of α. We compare the dTV reconstructions using FBS and Bregman iterations. For FBS, $\alpha = 10^{-5}$ provided the highest SSIM and for Bregman iterations, we stop after 2001 iterations.

5. Discussion and conclusions

We have analyzed synergistic reconstruction for multi-spectral CT reconstruction when a limited set of angles is observed. The proposed approach is based on combining information from all available energy channels into a polyenergetic image. This image is then included into the directional total variation regularizer for use in variational or iterative regularization.

We observed that the synergistic approach based on directional total variation is always superior to separate reconstruction using just total variation for both variational and iterative regularization. In addition, we consistently saw that linearized Bregman iterations converge faster to a desired solution than forward-backward splitting.

The observation that synergistic reconstruction can be faster than separate reconstruction is novel and interesting. Future work will be directed to fully understand this phenomenon.

Authors' Contributions: EC carried out the numerical computations and drafted the manuscript. MJE designed the project, advised EC and supported writing the manuscript. SS and AM acquiered and processed real data. All authors read and approved the manuscript.

Funding: MJE acknowledges support from the EPSRC (EP/S026045/1, EP/T026693/1), the Faraday Institution (EP/T007745/1) and the Leverhulme Trust (ECF-2019-478). EC acknowledges support from the CMM ANID PIA AFB170001 and Beca Doctorado Nacional Conicyt.

References

[1] J. Adler, H. Kohr, and O. Oktem. Operator discretization library (odl). *Software available from https://github. com/odlgroup/odl*, 2017. URL `https://github.com/odlgroup/odl`.

[2] A. M. Alessio and L. R. MacDonald. Quantitative material characterization from multi-energy photon counting ct. *Medical physics*, 40(3):031108, 2013. doi:10.1118/1.4790692.

[3] A. Beck and M. Teboulle. A fast iterative shrinkage-thresholding algorithm with application to wavelet-based image deblurring. In *2009 IEEE International Conference on Acoustics, Speech and Signal Processing*, pages 693–696. IEEE, IEEE, apr 2009a. doi:10.1109/icassp.2009.4959678.

[4] M. Benning and M. Burger. Ground states and singular vectors of convex variational regularization methods. *Methods and Applications of Analysis*, 20(4):295–334, 2013. doi:10.4310/maa.2013.v20.n4.a1.

[5] M. Benning, M. M. Betcke, M. J. Ehrhardt, and C.-B. Schönlieb. Choose your path wisely: gradient descent in a Bregman distance framework. *arXiv preprint arXiv:1712.04045*, 2017.

[6] T. Bonesky. Morozov's discrepancy principle and tikhonov-type functionals. *Inverse Problems*, 25 (1):015015, dec 2008. doi:10.1088/0266-5611/25/1/015015.

[7] L. Bungert, D. A. Coomes, M. J. Ehrhardt, J. Rasch, R. Reisenhofer, and C.-B. Schönlieb. Blind image fusion for hyperspectral imaging with the directional total variation. *Inverse Problems*, 34(4):044003, 2018. doi:10.1088/1361-6420/aaaf63.

[8] L. D. Chiffre, S. Carmignato, J.-P. Kruth, R. Schmitt, and A. Weckenmann. Industrial applications of computed tomography. *CIRP Annals*, 63(2):655–677, 2014. doi:10.1016/j.cirp.2014.05.011.

[9] R. Clackdoyle and M. Defrise. Tomographic reconstruction in the 21st century. *IEEE Signal Processing Magazine*, 27(4):60–80, 2010. doi:10.1109/msp.2010.936743.

[10] D. Colton, M. Piana, and R. Potthast. A simple method using morozov's discrepancy principle for solving inverse scattering problems. *Inverse Problems*, 13(6):1477, 1997. doi:10.1088/0266-5611/13/6/005.

[11] P. L. Combettes and J.-C. Pesquet. Proximal splitting methods in signal processing. In *Springer Optimization and Its Applications*, pages 185–212. Springer New York, 2011. doi:10.1007/978-1-4419-9569-8_10.

[12] P. L. Combettes and V. R. Wajs. Signal recovery by proximal forward-backward splitting. *Multiscale Modeling & Simulation*, 4(4):1168–1200, 2005. doi:10.1137/050626090.

[13] V. Corona, M. Benning, M. J. Ehrhardt, L. F. Gladden, R. Mair, A. Reci, A. J. Sederman, S. Reichelt, and C.-B. Schönlieb. Enhancing joint reconstruction and segmentation with non-convex Bregman iteration. *Inverse Problems*, 35(5):055001, 2019a. doi:10.1088/1361-6420/ab0b77.

[14] M. J. Ehrhardt. Multi-modality imaging with structure-promoting regularisers. pages 36–43, 2020. URL `http://arxiv.org/abs/2007.11689`.

[15] M. J. Ehrhardt and S. R. Arridge. Vector-valued image processing by parallel level sets. *IEEE Transactions on Image Processing*, 23(1):9–18, jan 2014. doi:10.1109/tip.2013.2277775.

[16] M. J. Ehrhardt and M. M. Betcke. Multicontrast mri reconstruction with structure-guided total variation. *SIAM Journal on Imaging Sciences*, 9(3):1084–1106, 2016. doi:10.1137/15m1047325.

[17] M. J. Ehrhardt, K. Thielemans, L. Pizarro, D. Atkinson, S. Ourselin, B. F. Hutton, and S. R. Arridge. Joint reconstruction of pet-mri by exploiting structural similarity. *Inverse Problems*, 31 (1):015001, 2014. doi:10.1088/0266-5611/31/1/015001.

[18] M. J. Ehrhardt, P. Markiewicz, M. Liljeroth, A. Barnes, V. Kolehmainen, J. S. Duncan, L. Pizarro, D. Atkinson, B. F. Hutton, S. Ourselin, K. Thielemans, and S. R. Arridge. PET reconstruction with an anatomical MRI prior using parallel level sets. *IEEE Transactions on Medical Imaging*, 35(9):2189–2199, sep 2016. doi:10.1109/tmi.2016.2549601.

[19] H. W. Engl, M. Hanke, and A. Neubauer. *Regularization of Inverse Problems*, volume 375. Springer Netherlands, 1996. doi:10.1007/978-94-009-1740-8.

[20] J. Frikel and E. T. Quinto. Characterization and reduction of artifacts in limited angle tomography. *Inverse Problems*, 29(12):125007, 2013. doi:10.1088/0266-5611/29/12/125007.

[21] H. Gao, H. Yu, S. Osher, and G. Wang. Multi-energy CT based on a prior rank, intensity and sparsity model (PRISM). *Inverse Problems*, 27(11):115012, oct 2011. doi:10.1088/0266-5611/27/11/115012.

[22] C. Groetsch. Comments on morozov's discrepancy principle. In *Improperly posed problems and their numerical treatment*, pages 97–104. Springer, 1983. doi:10.1007/978-3-0348-5460-3_7.

[23] K. Hamalainen, A. Kallonen, V. Kolehmainen, M. Lassas, K. Niinimaki, and S. Siltanen. Sparse tomography. *SIAM Journal on Scientific Computing*, 35(3):B644–B665, 2013. doi:10.1137/120876277.

[24] P. C. Hansen. *Discrete Inverse Problems*, volume 7. Society for Industrial and Applied Mathematics, jan 2010. doi:10.1137/1.9780898718836.

[25] M. Hintermüller, M. Holler, and K. Papafitsoros. A function space framework for structural total variation regularization with applications in inverse problems. *Inverse Problems*, 34(6):064002, apr 2018. doi:10.1088/1361-6420/aab586.

[26] A. Horé and D. Ziou. Image Quality Metrics: PSNR vs. SSIM. *2020 20th International Conference on Pattern Recognition*, Istanbul, 2010, pp. 2366—2369, doi:10.1109/ICPR.2010.579.

[27] Y. Hu, J. G. Nagy, J. Zhang, and M. S. Andersen. Nonlinear optimization for mixed attenuation polyenergetic image reconstruction. *Inverse Problems*, 35(6):064004, jun 2019. doi:10.1088/1361-6420/ab0131.

[28] R. H. Huesman. The effects of a finite number of projection angles and finite lateral sampling of projections on the propagation of statistical errors in transverse section reconstruction. *Physics in Medicine and Biology*, 22(3):511–521, may 1977. doi:10.1088/0031-9155/22/3/012.

[29] T. R. Johnson. Dual-energy ct: general principles. *American Journal of Roentgenology*, 199 (5_supplement):S3–S8, 2012. doi:10.2214/ajr.12.9116.

[30] J. P. Kaipio, V. Kolehmainen, M. Vauhkonen, and E. Somersalo. Inverse problems with structural prior information. *Inverse Problems*, 15(4):1111–1111, aug 1999. doi:10.1088/0266-5611/15/4/501.

[31] D. Kazantsev, J. S. Jørgensen, M. S. Andersen, W. R. Lionheart, P. D. Lee, and P. J. Withers. Joint image reconstruction method with correlative multi-channel prior for X-ray spectral computed tomography. *Inverse Problems*, 34(6):064001, 2018. doi:10.1088/1361-6420/aaba86.

[32] B. Krauss, B. Schmidt, and T. G. Flohr. Dual source CT. In *Dual Energy CT in Clinical Practice*, pages 11–20. Springer Berlin Heidelberg, sep 2010. doi:10.1007/174_2010_44.

[33] D. Lee, J. Lee, H. Kim, T. Lee, J. Soh, M. Park, C. Kim, Y. J. Lee, and S. Cho. A feasibility study of low-dose single-scan dual-energy cone-beam CT in many-view under-sampling framework. *IEEE Transactions on Medical Imaging*, 36(12):2578–2587, dec 2017. doi:10.1109/tmi.2017.2765760.

[34] M. M. Lell, J. E. Wildberger, H. Alkadhi, J. Damilakis, and M. Kachelriess. Evolution in computed tomography. *Investigative Radiology*, 50(9):629–644, sep 2015. doi:10.1097/rli.0000000000000172.

[35] A. Macovski, R. Alvarez, J.-H. Chan, J. Stonestrom, and L. Zatz. Energy dependent reconstruction in X-ray computerized tomography. *Computers in biology and medicine*, 6(4):325–336, 1976. doi:10.1016/0010-4825(76)90069-x.

[36] D. Marin, D. T. Boll, A. Mileto, and R. C. Nelson. State of the art: Dual-energy CT of the abdomen. *Radiology*, 271(2):327–342, may 2014. doi:10.1148/radiol.14131480.

[37] C. H. McCollough, G. H. Chen, W. Kalender, S. Leng, E. Samei, K. Taguchi, G. Wang, L. Yu, and R. I. Pettigrew. Achieving routine submillisievert ct scanning: report from the summit on management of radiation dose in ct. *Radiology*, 264(2):567–580, 2012. doi:10.1148/radiol.12112265.

[38] C. H. McCollough, S. Leng, L. Yu, and J. G. Fletcher. Dual- and multi-energy CT: Principles, technical approaches, and clinical applications. *Radiology*, 276(3):637–653, sep 2015. doi:10.1148/radiol.2015142631.

[39] V. A. Morozov. *Methods for solving incorrectly posed problems*. Springer Science & Business Media, 2012.

[40] F. Natterer. *The Mathematics of Computerized Tomography*. Society for Industrial and Applied Mathematics, jan 2001. doi:10.1137/1.9780898719284.

[41] S. Niu, G. Yu, J. Ma, and J. Wang. Nonlocal low-rank and sparse matrix decomposition for spectral CT reconstruction. *Inverse Problems*, 34(2):024003, jan 2018. doi:10.1088/1361-6420/aa942c.

[42] S. Osher, M. Burger, D. Goldfarb, J. Xu, and W. Yin. An iterative regularization method for total variation-based image restoration. *Multiscale Modeling & Simulation*, 4(2):460–489, jan 2005b. doi:10.1137/040605412.

[43] D. S. Rigie and P. J. L. Rivière. Joint reconstruction of multi-channel, spectral CT data via constrained total nuclear variation minimization. *Physics in Medicine and Biology*, 60(5):1741–1762, feb 2015. doi:10.1088/0031-9155/60/5/1741.

[44] J. Rogowska. *Handbook of Medical Imaging: Processing and Analysis Management*, volume 5. 2000.

[45] L. I. Rudin and S. Osher and E. Fatemi. Nonlinear total variation based noise removal algorithms *Physica D: Nonlinear Phenomena*, Elsevier BV, 60, 259–268, 1992. doi:10.1016/0167-2789(92)90242-f.

[46] T. Sarkar, D. Weiner, and V. Jain. Some mathematical considerations in dealing with the inverse problem. *IEEE Transactions on Antennas and Propagation*, 29(2):373–379, mar 1981. doi:10.1109/tap.1981.1142573.

[47] O. Scherzer, M. Grasmair, H. Grossauer, M. Haltmeier, and F. Lenzen. *Variational methods in imaging*. Springer, 2009.

[48] O. Semerci, N. Hao, M. E. Kilmer, and E. L. Miller. Tensor-based formulation and nuclear norm regularization for multienergy computed tomography. *IEEE Transactions on Image Processing*, 23(4):1678–1693, apr 2014. doi:10.1109/tip.2014.2305840.

[49] P. M. Shikhaliev. Energy-resolved computed tomography: first experimental results. *Physics in Medicine and Biology*, 53(20):5595–5613, sep 2008. doi:10.1088/0031-9155/53/20/002.

[50] P. M. Shikhaliev and S. G. Fritz. Photon counting spectral CT versus conventional CT: comparative evaluation for breast imaging application. *Physics in Medicine and Biology*, 56(7):1905–1930, mar 2011. doi:10.1088/0031-9155/56/7/001.

[51] D. Strong and T. Chan. Edge-preserving and scale-dependent properties of total variation regularization. *Inverse Problems*, 19(6):S165–S187, nov 2003. doi:10.1088/0266-5611/19/6/059.

[52] J. Toivanen, , A. Meaney, S. Siltanen, and V. K. and. Joint reconstruction in low dose multi-energy CT. *Inverse Problems & Imaging*, 14(4):607–629, 2020. doi:10.3934/ipi.2020028.

[53] Z. Wang, A. C. Bovik, H. R. Sheikh and E. P. Simoncelli. Image quality assessment: from error visibility to structural similarity. *IEEE Transactions on Image Processing*, vol. 13, no. 4, pp. 600-612, April 2004, doi:10.1109/TIP.2003.819861.

[54] Y.-W. Wen and R. H. Chan. Parameter selection for total-variation-based image restoration using discrepancy principle. *IEEE Transactions on Image Processing*, 21(4):1770–1781, apr 2012. doi:10.1109/tip.2011.2181401.

[55] Weiwen Wu, Yanbo Zhang, Qian Wang, Fenglin Liu, Fulin Luo, and Hengyong Yu. Spatial-spectral cube matching frame for spectral CT reconstruction. *Inverse Problems*, 34(10):104003, aug 2018. doi:10.1088/1361-6420/aad67b.

[56] D. Xu, D. A. Langan, X. Wu, J. D. Pack, T. M. Benson, J. E. Tkaczky, and A. M. Schmitz. Dual energy ct via fast kvp switching spectrum estimation. In *Medical Imaging 2009: Physics of Medical Imaging*, volume 7258, page 72583T. International Society for Optics and Photonics, 2009. doi:10.1117/12.811650.

[57] Wotao Yin, Stanley Osher, Donald Goldfarb, and Jerome Darbon. Bregman iterative algorithms for ℓ_1-minimization with applications to compressed sensing. *SIAM Journal on Imaging Sciences*, 1(1):143–168, jan 2008. doi:10.1137/070703983.

[58] W. Yin. Analysis and generalizations of the linearized Bregman method. *SIAM Journal on Imaging Sciences*, 3(4):856–877, 2010. doi:10.1137/090760350.

[59] Y. Zou and M. D. Silver. Analysis of fast kV-switching in dual energy CT using a pre-reconstruction decomposition technique. In J. Hsieh and E. Samei, editors, *Medical Imaging 2008: Physics of Medical Imaging*, volume 6913, page 691313. International Society for Optics and Photonics, SPIE, mar 2008. doi:10.1117/12.772826.